Bull Volcanol (2011) 73:679–697
DOI 10.1007/s00445-010-0433-0

RESEARCH ARTICLE

# The May 2005 eruption of Fernandina volcano, Galápagos: The first circumferential dike intrusion observed by GPS and InSAR

**William W. Chadwick Jr · Sigurjon Jónsson · Dennis J. Geist · Michael Poland · Daniel J. Johnson · Spencer Batt · Karen S. Harpp · Andres Ruiz**

Received: 29 May 2010 / Accepted: 12 November 2010 / Published online: 15 December 2010


**Abstract** The May 2005 eruption of Fernandina volcano, Galápagos, occurred along circumferential fissures parallel to the caldera rim and fed lava flows down the steep southwestern slope of the volcano for several weeks. This was the first circumferential dike intrusion ever observed by both InSAR and GPS measurements and thus provides an opportunity to determine the subsurface geometry of these enigmatic structures that are common on Galápagos volcanoes but are rare elsewhere. Pre- and post- eruption ground deformation between 2002 and 2006 can be modeled by the inflation of two separate magma reservoirs beneath the caldera: a shallow sill at ~1 km depth and a deeper point-source at ~5 km depth, and we infer that this system also existed at the time of the 2005 eruption. The co-eruption deformation is dominated by uplift near the 2005 eruptive fissures, superimposed on a broad subsidence centered on the caldera. Modeling of the co-eruption deformation was performed by including various combinations of planar dislocations to simulate the 2005 circumferential dike intrusion. We found that a single planar dike could not match both the InSAR and GPS data. Our best-fit model includes three planar dikes connected along hinge lines to simulate a curved concave shell that is steeply dipping (~45–60°) toward the caldera at the surface and more gently dipping (~12–14°) at depth where it connects to the horizontal sub-caldera sill. The shallow sill is underlain by the deep point source. The geometry of this modeled magmatic system is consistent with the petrology

Editorial responsibility: M. Ripepe

Daniel J. Johnson (deceased)

**Electronic supplementary material** The online version of this article (doi:10.1007/s00445-010-0433-0) contains supplementary material, which is available to authorized users.

W. W. Chadwick Jr (✉)
Oregon State University/NOAA, Hatfield Marine Science Center,
Newport, OR 97365, USA
e-mail: bill.chadwick@noaa.gov

S. Jónsson
KAUST - King Abdullah University of Science and Technology,
Thuwal 23955, Saudi Arabia

D. J. Geist · S. Batt
Department of Geological Sciences, University of Idaho,
Moscow, ID 83844, USA

M. Poland
Hawaiian Volcano Observatory, USGS,
Volcano, HI 96718, USA

D. J. Johnson
Department of Geology, University of Puget Sound,
Tacoma, WA 98416, USA

K. S. Harpp
Department of Geology, Colgate University,
Hamilton, NY 13346, USA

A. Ruiz
Instituto Geofísico, Escuela Politécnica Nacional,
Quito, Ecuador

of Fernandina lavas, which suggest that circumferential eruptions tap the shallowest parts of the system, whereas radial eruptions are fed from deeper levels. The recent history of eruptions at Fernandina is also consistent with the idea that circumferential and radial intrusions are sometimes in a stress-feedback relationship and alternate in time with one another.

**Keywords** Circumferential dike intrusion · Ground deformation · Kinematic modeling · Magma reservoirs

## Introduction

Fernandina is the westernmost and most active volcano in the Galápagos archipelago (Fig. 1) and is on the leading edge of the Galápagos hotspot (Allan and Simkin 2000). Fernandina perhaps best exhibits the distinctive spatial pattern of eruptive fissures that characterizes young Galápagos volcanoes, consisting of circumferential fissures within a few km of the summit caldera margins and radial fissures lower on the flanks (McBirney and Williams 1969; Simkin 1984; Chadwick and Howard 1991). The mechanism controlling this pattern of dike intrusion is not clear but probably involves a combination of stresses imparted by pressurized magma bodies and gravitational forces acting on the outer slopes and calderas (Chadwick and Dieterich 1995). This hypothesis has motivated geodetic monitoring in the Galápagos. Circumferential dikes are particularly puzzling and intriguing, because they are relatively common in deeply dissected volcanic systems (Anderson 1936; Bailey and Maufe 1960; Walker 1993; Johnson et al. 2002) but rare at active volcanoes outside Galápagos (Chadwick and Howard 1991). In fact, prior to the results reported here, no circumferential dike intrusion had been "caught in the act" by a monitoring network.

Fernandina has had at least 25 historical eruptions (Simkin 1984; Simkin and Siebert 1994, http://www.volcano.si.edu/), including a radial eruption on the SW flank in 1995 (Jónsson et al. 1999; Rowland et al. 2003), followed by a circumferential eruption on the SW summit in May 2005, which is the focus of this paper (Fig. 2). A subsequent radial eruption occurred on the SW flank in

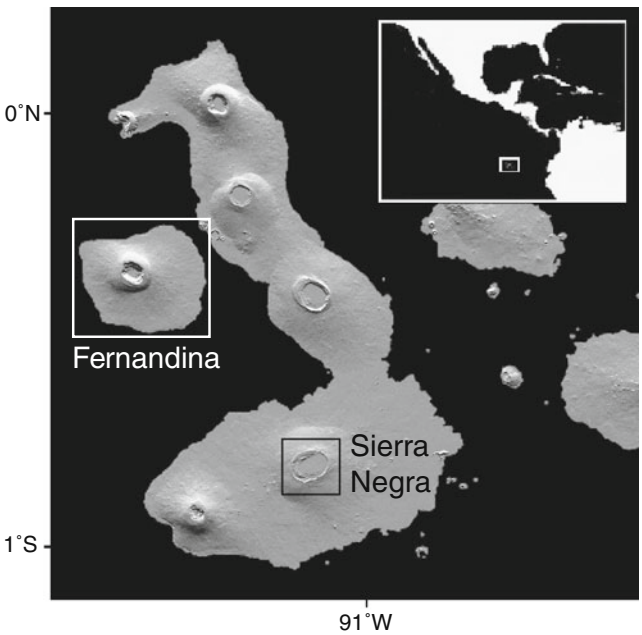


**Fig. 1** Map showing location of Fernandina volcano in the Galápagos islands (*white box*), and neighboring Sierra Negra volcano (*black box*)

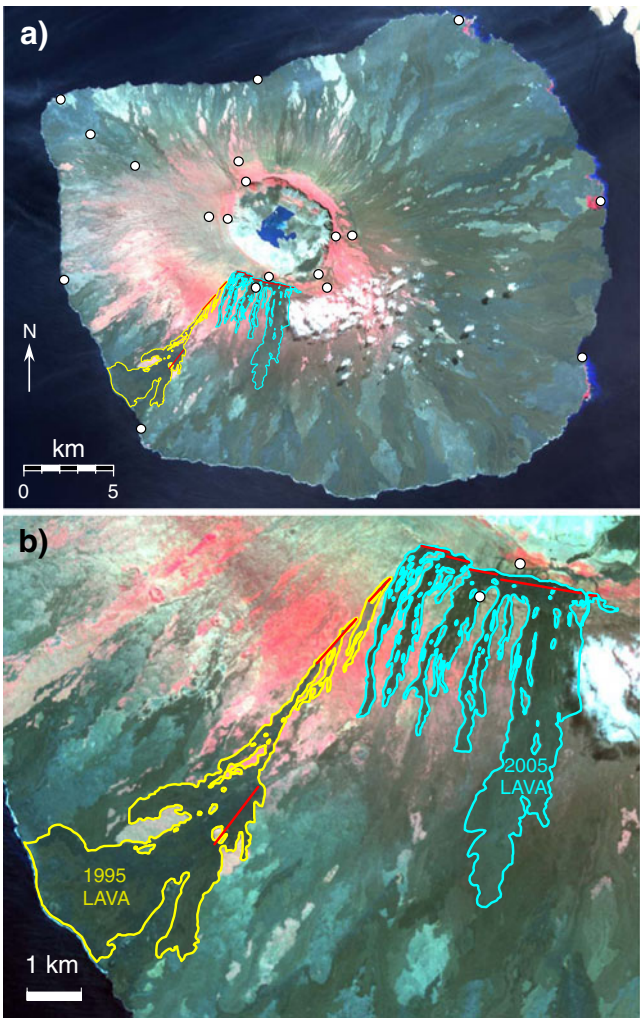


**Fig. 2** Multispectral ASTER satellite image used to map the 1995 and 2005 lava flows (1995=yellow; 2005=blue) and eruptive fissures (*red*) SW of the summit caldera. The image has a 15-m spatial resolution and was acquired June 21, 2007. The data are false color, with near-IR, red, and green bands displayed in red, green, and blue, respectively. Vegetation appears as shades of *red and pink*, and barren lava and ash appear as *tan, cyan, and greenish black*. Campaign GPS stations are shown as *white dots* and are labeled in Fig. 3

April 2009 (Bagnardi et al. 2009; Bagnardi and Amelung 2010), but will not be discussed here.

Although they are very active volcanoes, geophysical studies in Galápagos have been limited due to their remote location, lack of infrastructure, and logistical challenges. The first geodetic studies on Fernandina involved the application of interferometric synthetic aperture radar (InSAR) data starting in the 1990s. Jónsson et al. (1999) interpreted the deformation signal from the 1995 flank eruption as being due to the opening of a shallowly dipping dike, and Amelung et al. (2000) found evidence for post-eruption re-inflation in the years following that eruption. The first ground-based geodetic measurements began in 2000 when a campaign-GPS network was established, and subsequent reoccupations of the network in 2001 and 2002 showed continued inflation (Geist et al. 2006a). The GPS network was reoccupied again after the 2005 eruption in July 2006.

Here, we present an analysis of surface deformation associated with the May 2005 eruption at Fernandina, focusing on kinematic modeling of InSAR and campaign-GPS data. We also report on the petrology and geochemistry of the eruptive products and the evidence they provide for the magmatic plumbing system at Fernandina. The 2005 event is significant because it is the first eruption for which the three-dimensional orientation of a circumferential dike is strongly constrained by both ground- and satellite-based geodetic data, and thus has implications for how its emplacement relates to the underlying magmatic plumbing system at the volcano. Our results suggest that the dike that fed the 2005 eruption was shaped like a curved shell, concave toward the caldera in both a horizontal and a vertical sense, and tapped the shallowest of at least two magma reservoirs at different depths beneath the summit caldera.

## The May 2005 eruption

The 2005 eruption at Fernandina started on 13 May at ~0935 (local time) and lasted until about 29 May, although most of the lava erupted during the first few days (Smithsonian Institution 1995–2009). The circumferential eruptive fissure consists of 5 right-stepping *en echelon* segments that individually strike 095–102°, while the overall trend of the fissures is 106°, nearly perpendicular to the 1995 radial eruptive fissures (which have an azimuth of 037–042°; Fig. 2). The western end of the 2005 eruptive fissure is 800 m northeast of the upslope end of the 1995 line of fissures, and from here the 2005 fissures extend east-southeastward for 3.3 km (Fig. 2). The 2005 eruptive fissures are located on the summit plateau between the southern caldera rim and the steep upper slopes of the volcano, and they are roughly parallel to, and 250–350 m south of, the 1982 eruptive fissures, which were also circumferential (Smithsonian Institution 1995–2009). The 2005 lavas are shelly pahoehoe and a'a on the summit plateau where they ponded before flowing southward through gaps in an older outboard circumferential crater row and descending the steep southern slope in five major a'a lava streams. The eastern end of the 2005 eruptive fissures produced the largest lava flow, which extended 6 km from the vents and reached within 4.5 km of the coast. Mapping from an ASTER satellite image (Fig. 2) indicates an area for the 2005 flows of 9.4 $km^2$ and an estimated dense-rock equivalent (DRE) volume of $14\times10^6$ $m^3$ (assuming an average thickness of 2 m and 25% void space, based on field observations). The 2005 lavas cover a slightly larger subaerial area than, but have about a quarter the volume of, the 1995 lavas, mainly because the 2005 eruption was much shorter-lived (16 vs. 73 days), and the lava flows are thinner because they are primarily on steep slopes. The subaerial 1995 flows on the SW flank have an area of 8.4 $km^2$ based on the ASTER imagery (Fig. 2), and an estimated DRE volume of $42\times10^6$ $m^3$, as calculated by Rowland et al. (2003); these values are minima because they do not include lava briefly erupted in the caldera at the start of the 1995 eruption and an unknown but substantial volume of lava that flowed into the ocean.

The only seismic data available are those from the global seismic network. Following a period of 5 years with no detected events, three moderate earthquakes occurred within 100 km of Fernandina in the months preceding the May 2005 eruption: an $m_b$ 4.0 on 23 February, an $m_b$ 4.6 on 16 April, and an $m_b$ 5.0 on 11 May (http://earthquake.usgs.gov/regional/neic/). These earthquakes are poorly located due to the lack of nearby seismic stations; thus, their significance remains ambiguous. Similar episodes of moderate earthquakes preceding eruptions at Fernandina have been noted in the past (Filson et al. 1973; Chadwick et al. 1991; Rowland et al. 2003) and suggest they are related to some (unknown) process of structural accommodation and faulting during major subsurface magma movements. Moderate earthquake swarms are also associated with eruptions at neighboring Sierra Negra volcano, where they have been documented to occur on an active intra-caldera fault system (Chadwick et al. 2006; Jónsson 2009).

## GPS data

A campaign-GPS network of 20 stations was established at Fernandina in January 2000 (Figs. 2 and 3), consisting of 7 stations along the coast, 11 stations on the rim of the

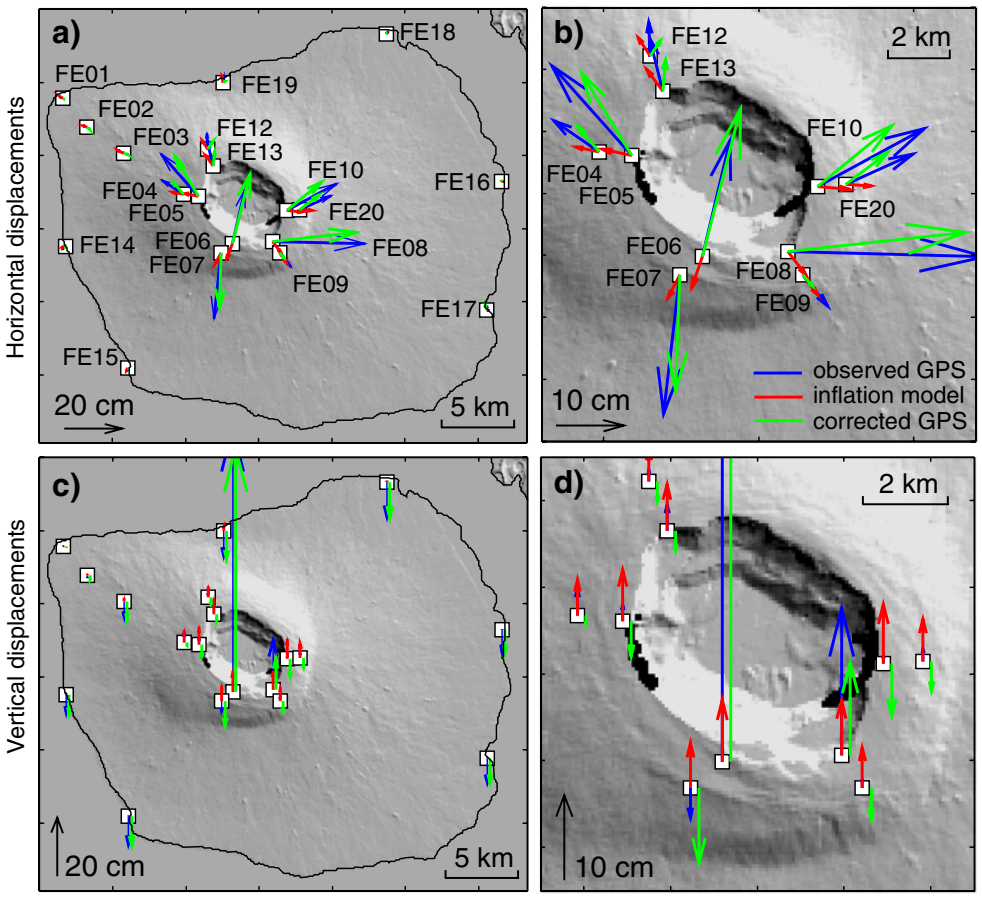


**Fig. 3** GPS displacements (blue vectors) measured between surveys in June 2002 and June 2006, showing both (**a**–**b**) horizontal and (**c**–**d**) vertical displacements, relative to station FE01 on the NW coast (**a** and **c** show entire island; **b** and **d** show detail around the caldera). Red vectors are predicted displacements modeled from pre- and post-eruption inflation observed with InSAR (Fig. 5), which is subtracted from the measured displacements to estimate co-eruption deformation at the GPS stations (green vectors). These corrected GPS displacements are then used in the co-eruption modeling

caldera, and 2 stations between the summit and NW coast (Geist et al. 2006a). There are no stations inside the 800-m-deep caldera due to extremely difficult access. The GPS network was re-occupied in January 2001 and June 2002, revealing a modest inflation signal modeled by Geist et al. (2006a) as due to magma accumulation at a rate of 0.35–$0.85 \times 10^6$ $m^3$/year within a magma reservoir at a depth of 1–2 km.

The campaign-GPS stations on the upper flanks were installed in pairs, with benchmarks on the caldera rim and ~1 km downslope, in the hope of recording the deformation associated with any future circumferential intrusions between stations. In fact, the 2005 eruptive fissures broke the surface about mid-way between stations FE06 and FE07 (Figs. 2 and 3). The GPS network was re-occupied in June 2006, and the data were processed using the BERNESE software (Hugentobler et al. 2001) following the procedures outlined by Geist et al. (2006a).

The 2002–2006 displacements (Table 1) reveal that stations FE06 and FE07 spread apart by 42 cm, with FE06 (the inboard station) uplifted by 94 cm relative to FE07 (Fig. 3). Measurement uncertainty is estimated to be ±3 mm for horizontal and ±1 cm for vertical displacements (Geist et al. 2006a). There is some ambiguity about what reference frame to use in such a network, and we have chosen to assume that station FE01 (on the NW coast) had zero displacement. This choice of datum results in the other coastal stations showing a relative subsidence of 6–12 cm, which is not apparent in the InSAR data and perhaps implies a larger source of error in the vertical GPS displacements. Nevertheless, this choice of datum does not significantly affect the modeling results below (i.e. choosing FE16 as the datum yields almost identical model results but with a slightly worse fit to the data). As expected, the largest horizontal displacements were measured on the summit plateau, closest to the eruption site and the caldera.

## InSAR data

Interferograms were made from SAR data collected by the ASAR instrument on the European Space Agency's ENVISAT satellite before and after the May 2005 eruption. InSAR can resolve ground movement in the line-of-sight (LOS) direction between the satellite and the ground (Zebker et al. 2000), whereas GPS provides three dimensional displacements. We utilized two independent tracks of

**Table 1** Original and corrected GPS displacements, in centimeters

| GPS station name | Original measured GPS displacements, relative to station FE01 | | | Predicted displacements from pre- and post-eruption sill and point-source model | | | Corrected GPS displacements, used in co-eruption modeling | | |
|---|---|---|---|---|---|---|---|---|---|
| | East | North | Vertical | East | North | Vertical | East | North | Vertical |
| FE01 | 0 | 0 | 0 | −0.8 | 0.5 | 0.4 | 0.8 | −0.5 | −0.4 |
| FE02 | −0.1 | −0.1 | −0.9 | −1.2 | 0.6 | 0.6 | 1.1 | −0.7 | −1.5 |
| FE03 | −0.2 | 0.3 | −5.2 | −1.8 | 0.8 | 1.1 | 1.6 | −0.5 | −6.3 |
| FE04 | −7.3 | 5.0 | 3.2 | −3.8 | 0.7 | 4.1 | −3.6 | 4.3 | 0.9 |
| FE05 | −12.8 | 14.5 | 1.9 | −4.7 | 1.1 | 6.0 | −8.1 | 13.4 | −4.1 |
| FE06 | 4.4 | 18.7 | 90.8 | −1.7 | −5.1 | 7.2 | 6.1 | 23.8 | 83.6 |
| FE07 | −2.6 | −22.5 | −3.4 | −1.9 | −3.8 | 5.3 | −0.7 | −18.7 | −8.7 |
| FE08 | 31.7 | −0.8 | 17.0 | 3.0 | −3.9 | 6.4 | 28.7 | 3.1 | 10.7 |
| FE09 | 4.0 | −5.0 | 1.0 | 2.4 | −3.2 | 4.6 | 1.6 | −1.8 | −3.6 |
| FE10 | 17.2 | 9.3 | 0.9 | 5.3 | −0.5 | 6.9 | 11.9 | 9.8 | −6.0 |
| FE12 | −0.2 | 5.5 | 1.3 | −1.9 | 3.0 | 3.7 | 1.7 | 2.5 | −2.4 |
| FE13 | −2.2 | 8.6 | 3.0 | −2.6 | 3.5 | 5.3 | 0.4 | 5.1 | −2.3 |
| FE14 | −1.2 | −1.0 | −6.0 | −1.2 | −0.3 | 0.5 | −0.1 | −0.7 | −6.5 |
| FE15 | −0.3 | −1.0 | −9.6 | −0.6 | −0.9 | 0.4 | 0.3 | −0.1 | −10.0 |
| FE16 | 0.2 | 1.2 | −8.4 | 0.6 | −0.3 | 0.2 | −0.4 | 1.5 | −8.6 |
| FE17 | 0.3 | 0.6 | −7.6 | 0.7 | 0.1 | 0.2 | −0.4 | 0.5 | −7.8 |
| FE18 | 0.7 | 0.9 | −12.0 | 0.6 | 0.7 | 0.3 | 0.1 | 0.2 | −12.3 |
| FE19 | 0.3 | 2.4 | −8.5 | −0.4 | 2.0 | 1.2 | 0.7 | 0.4 | −9.7 |
| FE20 | 10.8 | 4.9 | 1.5 | 4.1 | −0.2 | 4.9 | 6.7 | 5.1 | −3.4 |

ASAR data over Fernandina (Table 2), one ascending and the other descending. "Ascending" and "descending" refer to the satellite orbit direction from the ground, northward or southward respectively, and because SAR data are collected from off-nadir, the two tracks differ in their LOS look angles and azimuths. Interferograms of Fernandina were corrected for topographic effects using the TOPSAR digital elevation model, which is based on data collected in 1993 (Rowland 1996). All the interferograms suffer to varying degrees from loss of phase coherence due to vegetation, steep slopes, large deformation signals, and resurfacing by lava, all of which are most problematic in and around the summit caldera (Fig. 4).

Because the time spanned by the GPS surveys was 4.5 years, the GPS displacements include a mix of three different deformation signals: 1) pre-eruption inflation

**Table 2** Information and dates of Envisat SAR images (IS-2) used to create the interferograms used in this study and dates of GPS campaigns at Fernandina. The ascending images were acquired from track 61 and descending images from track 412

| Radar scene 1/GPS surveys | Date 1 | Radar scene 2 | Date 2 | Time interval (months) | Perpendicular Baseline (m) | Subsampled points |
|---|---|---|---|---|---|---|
| Pre-eruption interferograms | | | | | | |
| Asc., orbit 4624 | Jan 18, 2003 | Asc., orbit 15646 | Feb 26, 2005 | 25 | 79 | 325 |
| Desc., orbit 5977 | April 22, 2003 | Desc., orbit 16498 | April 26, 2005 | 24 | 424 | 359 |
| Co-eruption interferograms | | | | | | |
| Asc., orbit 16648 | May 7, 2005 | Asc., orbit 17650 | July 16, 2005 | 2 | 120 | 584 |
| Desc., orbit 16498 | April 26, 2005 | Desc., orbit 18502 | Sept. 13, 2005 | 4.5 | 105 | 663 |
| Post-eruption interferograms | | | | | | |
| Asc., orbit 18151 | August 20, 2005 | Asc., orbit 24163 | October 14, 2006 | 14 | 110 | 394 |
| Desc., orbit 18001 | August 9, 2005 | Desc., orbit 24514 | Nov. 7, 2006 | 15 | 183 | 542 |
| GPS campaigns | June 4–13, 2002 | | July 7–12, 2006 | 49 | | 3×21 |

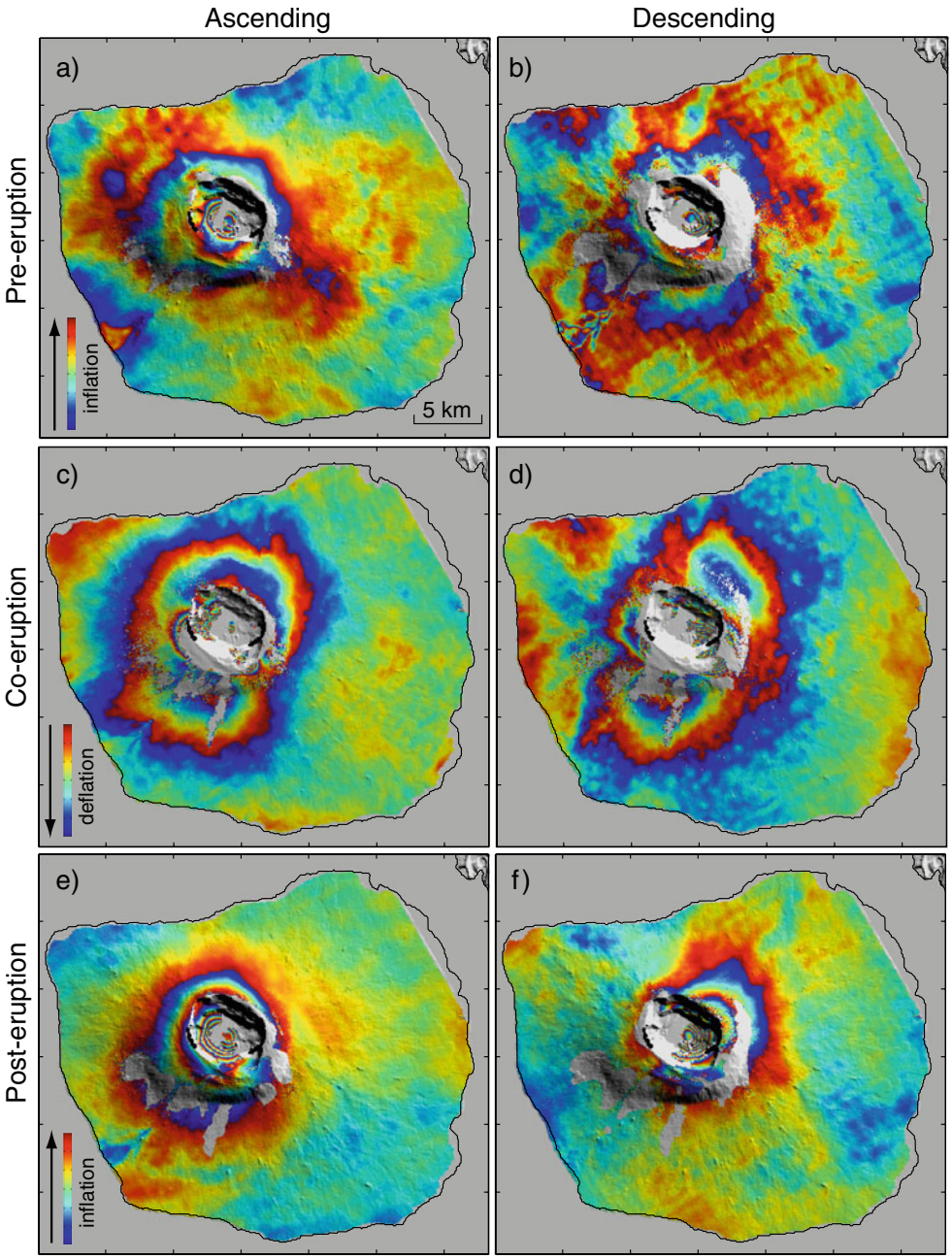


**Fig. 4** InSAR data of Fernandina used in this study (Table 2), showing (**a**–**b**) pre- eruption, (**c**–**d**) co-eruption, and (**e**–**f**) post-eruption deformation. For each time period, both an ascending (left) and a descending (right) interferogram are shown. One color cycle represents 2.81 cm of line-of-sight (LOS) ground displacement. Lack of color indicates areas of incoherence, which are masked in the interferograms for clarity. The order of color progression shows whether the deformation is uplift or subsidence (toward or away from the radar satellite). The inward progression of yellow-to-red-to-blue concentric to the caldera in (**a**–**b**) and (**e**–**f**) indicates inflation during the pre- and post-eruption intervals, whereas the blue-to-red-to-yellow order on the volcano flanks in (**c**–**d**) indicates broad deflation (in addition to dike-related uplift) during the co-eruption period

(June 2002–May 2005), 2) co-eruption deflation and dike-emplacement, and 3) post-eruption inflation (May 2005–June 2006). To separate these signals, ascending and descending interferograms spanning pre-eruption, co-eruption, and post-eruption time intervals were constructed (Fig. 4), resulting in six different interferograms for use in this study (Table 2). Our strategy was to use the InSAR data to characterize the simpler pre- and post-eruption inflation signals and subtract those displacements from the GPS results, thereby isolating the more complicated co-eruption deformation and facilitating modeling for source parameters using both types of data. We chose radar scenes acquired as close to the dates of the GPS campaigns and the eruption as possible, but the two data sets are not exactly coincident (Table 2).

## Petrologic methods

Samples of early-erupted 2005 lava and tephra were analyzed for major and trace elements by XRF and ICPMS using the methods of Johnson et al. (1999) and Harpp et al. (2003). The early-erupted samples were taken from scoria mounds that mark parts of the fissure that

stopped erupting on the first day. The late-erupted samples come from near the vent of the last-erupting fissure segment. Samples of the 1995 lava were taken from near the coast for comparison.

## Modeling results

To constrain the source of surface deformation associated with the 2005 eruption of Fernandina, we estimated parameters of deformation sources in an elastic halfspace through non-linear optimization of the GPS and InSAR data (Jónsson et al. 2002; Chadwick et al. 2006; Jónsson 2009). However, before conducting the optimizations, we estimated data errors in all six interferograms in order to build covariance matrices and properly weight the InSAR data in the modeling. To do that, we generated sample variograms and covariograms based on the non-deforming part within each interferogram and then fitted exponentially decaying covariance functions to the sample covariograms (Sudhaus and Jónsson 2009). From each covariance function we built a data covariance matrix that we used to internally weight the corresponding InSAR dataset, as well as weight it against the GPS data and other interferograms. We also used the covariance functions to generate multiple sets of synthetic noise that we added to the original data, and ran hundreds of optimizations using noise-modified data sets. This procedure helps to statistically determine how well the deformation sources are constrained by the modeling.

Our modeling incorporates three potential idealized deformation sources: sills, dikes, and point sources. A shallow source of inflation or deflation centered beneath the caldera is modeled as a horizontal sill (a planar dislocation with uniform opening, as in Okada (1992)). This is consistent with previous modeling of shallow inflating magma reservoirs at nearby Sierra Negra volcano (Fig. 1), which found that a sill-like geometry reproduces the details of observed deformation signals better than a point source (Amelung et al. 2000; Jónsson et al. 2005; Yun et al. 2006). Because there is evidence for a separate, deeper source of inflation/deflation at Fernandina (discussed below) whose exact geometry is poorly constrained, we also incorporated a point source (Mogi 1958) beneath the sub-caldera sill. The 2005 dike is modeled as either a single rectangular plane with uniform opening (Okada 1992) or as multiple planes connected along hinge lines to simulate a curving dike.

The modeling assumes an elastic half-space with no topography and a Poisson's ratio of 0.25. Therefore, the best-fit depths we report for the deformation sources are relative to the flat upper surface of the half-space, which is effectively a mean elevation within the study area (the GPS and InSAR data are projected onto this mean-elevation surface). Interferograms were subsampled using a quadtree algorithm (Jónsson et al. 2002) to reduce the large number of data values and facilitate combined modeling with GPS results. In the optimizations, each of the model parameters for the deformation sources can be held fixed or allowed to float (for a point source: position, depth, and volume change; for the planar dislocation sources: position, depth, strike, dip, length, width, and opening). We then used a simulated annealing algorithm to vary each of the unknowns within specified bounds while seeking a solution that minimizes the difference between the observed displacements and those predicted by the model. In the interferograms, where patches of coherent phase exist within the caldera but are disconnected from the rest of the volcano due to surrounding areas of incoherence, we allowed the coherent patches to float vertically in our modeling and solved for their best-fit position as an additional parameter. We found that it was difficult to model the complex co-eruption deformation without making some assumptions, because permitting all the source parameters to float yielded geologically unrealistic results, such as dikes not coinciding with the eruptive fissures at the surface, or sill and point sources located outside the caldera. Consequently, we chose to fix some of the source parameters to values that could be justified geologically (described below and in Tables 3 and 4). This reduced the number of unknowns, allowing us to focus on specific parts of the problem and draw meaningful qualitative and quantitative conclusions.

### Analysis of pre- and post-eruption deformation using InSAR data only

Qualitatively, for both the pre- and post-eruption time intervals, InSAR data show a more or less circular and radially symmetric inflation signal centered on the caldera. Part of the source of the uplift appears to be relatively shallow because the fringes are concentrated inside the caldera (Fig. 5). LOS displacements are up to 17 cm inside the caldera in the pre-eruption interferograms and up to 25 cm during the post-eruption time period. The fringes on the lower volcano flanks are small in amplitude and presumably reflect atmospheric effects and errors (in case of Fig. 4b) in the TOPSAR DEM (Yun et al. 2005), except over the 1995 and 2005 lava flows where subsidence or incoherence is observed due to cooling, contraction, and perhaps downslope creep. However, a single shallow source does not explain all of the observed deformation signal, because some fringes extend outside the caldera, suggesting that a deeper deformation source also exists. The evidence for this is even clearer in the co-eruption interferograms, which are characterized by a broad deflation signal extending far outside the caldera (with LOS displacements

**Table 3** Summary of estimated model parameters for the pre- and post-eruption time periods, using InSAR data only. Parameter confidence bounds (1-sigma) are shown in brackets

| Preferred deformation model: one shallow sill, and one deep point-source[a] | | |
|---|---|---|
| | Pre-eruption (RMS=0.86 cm) | Post-eruption (RMS=1.18 cm) |
| Sill depth (km) | 0.93 [0.88, 0.97] | 1.18 [1.13, 1.23] |
| Sill length (km) | 2.46 [2.41, 2.49] | 2.46 [2.41, 2.51] |
| Sill width (km) | 1.75 [1.72, 1.79] | 1.66 [1.63, 1.70] |
| Sill opening (m) | 0.18 [0.17, 0.19] | 0.34 [0.30, 0.36] |
| Sill volume change ( $\times 10^6$ $m^3$) | 0.75 [0.72, 0.80] | 1.36 [1.25, 1.47] |
| Deep point-source depth (km) | 6.07 [5.40, 6.87] | 3.92 [3.45, 4.44] |
| Point-source vol. change ( $\times 10^6$ $m^3$) | 5.07 [4.45, 5.83] | 2.93 [2.54, 3.30] |
| Alternative deformation model: two point-sources, one shallow, one deep | | |
| | Pre-eruption (RMS=1.03 cm) | Post-eruption (RMS=1.25 cm) |
| Shallow point-source depth (km) | 1.55 [1.52, 1.58] | 1.52 [1.47, 1.54] |
| Volume change ( $\times 10^6$ $m^3$) | 1.60 [1.53, 1.70] | 2.50 [2.40, 2.61] |
| Deep point-source depth (km) | 10.5 [8.77, 14.3] | 10.1 [7.70, 17.1] |
| Volume change ( $\times 10^6$ $m^3$) | 4.84 [3.69, 7.07] | 1.10 [0.64, 2.20] |

[a] Sill strike is held fixed at 106°, which is the strike of the 2005 eruptive fissures. Sill geometry used for the co-eruption modeling has the average of the other pre- and post-eruption parameters (strike=106°, dip=0°, depth=1.06 km, length=2.46 km, width=1.71 km). Point-source location used in the co-eruption modeling is the average of the pre- and post-eruption sill/point-source results (a depth of 5.0 km at 0.3717°S and 91.5398°W, near the center of the caldera)

of up to 5.5 cm; Figs. 4e & f), again suggesting a second deeper source of volume change beneath the caldera. Therefore, our preferred model for the pre- and post-eruption InSAR data assumes two deformation sources, a shallow (1–5 km depth) sill and a deep (5–15 km depth) point-source. The size, location, and depth of the shallow sill and deep point-source were allowed to float in the models, and the results indicate that both are centered beneath the caldera.

Separate modeling of the pre- and post-eruption time intervals yields similar results (Table 3; Fig. 5). The error analysis we performed with the InSAR data allows us to quantify model parameter uncertainties due to errors in the data, with 68% and 95% histogram quantiles roughly equivalent to 1-sigma and 2-sigma uncertainties in those parameters. For the pre-eruption interval, the 1-sigma depth bounds are 0.9–1.0 km for the sill and 5.4–6.9 km for the point-source (Table 3). For the post-eruption period, the 1-sigma depth bounds are 1.1–1.2 km for the sill and 3.5–4.4 km for the point source. Thus, a sill at a depth of ~1 km and a point-source at ~5 km depth can explain most of the deformation observed during both the pre- and post-eruption time intervals, and we use the average of the pre- and post-eruption parameters to model the co-eruption time period (below).

For comparison, we also conducted the modeling assuming the deformation was due to two point-sources (one shallow and one deep) instead of a sill/point-source combination. In general, this gave similar results, although the depths of the two sources are different: the shallow source is at ~1.5 km and the deeper one is between ~10 km depth (Table 3). The model fit to the InSAR data is significantly better for the shallow sill and deep point-source combination, so we have chosen that as our preferred model for the sub-caldera magmatic system. An independent study of InSAR data collected over a longer time interval (1992–2010) also concluded that Fernandina has multiple magma reservoirs at different depths below the caldera (Bagnardi et al. 2009; Bagnardi and Amelung 2010), providing support for this conclusion.

Between early 2003 and the start of the 2005 eruption, model results above suggest an inflation rate of $0.4\times10^6$ $m^3$/year in the shallow sill and $2.5\times10^6$ $m^3$/year in the deeper source. The value for the shallow reservoir is about half the rate determined by Geist et al. (2006a) between 2000 and 2002, and about a third of the average rate of supply necessary between 1995 and 2005 to account for the volume of the 2005 lava flow (estimated at $14\times10^6$ $m^3$). The rate of inflation between the 2005 eruption and late 2006 was $1.2\times10^6$ $m^3$/year in the shallow source and $2.5\times10^6$ $m^3$/year in the deeper source. The fact that the shallow inflation rate after the eruption is three times greater than before the eruption is consistent with studies at other volcanoes where inflation rates are highest right after eruptions and decrease with time (Dvorak and Okamura 1987; Lu et al. 2000; Ruiz et al. 2007; Nooner and Chadwick 2009). This can be explained by a smaller pressure gradient between the shallow and deep reservoirs before the eruption (when the shallow reservoir is presumably full and pressurized) and a higher gradient after the eruption (after the shallow reservoir has

**Table 4** Summary of source parameters from modeling results for the co-eruption time period

Co-eruption: 1 surface dike

| | GPS-only, Fig. S1 | InSAR-only, Fig. S2 | GPS/InSAR, Fig. S3 |
|---|---|---|---|
| Dike length (km) | 3.30[a] | 4.21 | 3.30[a] |
| Dike width (km) | 2.33 | 2.21 | 2.76 |
| Dike depth, top edge (km) | 0.0[a] | 0.48 | 0.0[a] |
| Dike dip (°) | 58.1 | 26.1 | 33.8 |
| Dike opening (m) | 0.69 | 1.04 | 1.00 |
| Sill opening (m) | 4.78 | −0.75 | −0.15 |
| Sill ΔV ( × $10^6$ $m^3$) | 20.0 | −0.31 | −0.61 |
| Point-source ΔV ( ×$10^6$ $m^3$) | −8.39 | −8.88 | −3.02 |
| RMS – GPS (cm) | 7.44 | 10.8 | 6.32 |
| RMS – InSAR (cm) | 75.8 | 2.64 | 5.06 |

Co-eruption: 2 dikes, constrained by both GPS and InSAR data, Figs. 6 and 7

| | Surface dike | Hinge dike | East dike | Sill | Point source |
|---|---|---|---|---|---|
| Length (km) | 3.30[a] | 4.32 | n/a | 2.46[a] | – |
| Width (km) | 0.79 | 1.59 | n/a | 1.71[a] | – |
| Depth (km) | 0.0[a] | 0.67 | n/a | 1.06[a] | 5.0[a] |
| Dip (°) | 58.0[a] | 14.0 | n/a | 0.0[a] | – |
| Opening (m) | 0.65 | 0.94 | n/a | 0.22 | – |
| ΔV ( × $10^6$ $m^3$) | 1.70 | 6.45 | n/a | 0.92 | −6.2 |
| RMS - GPS=6.20 cm; RMS - InSAR=4.61 cm | | | | | |

Co-eruption: 3 dikes, constrained by both GPS and InSAR data, Figs. 8 and 9

| | Surface dike | Hinge dike | East dike | Sill | Point source |
|---|---|---|---|---|---|
| Length (km) | 3.30[a] | 4.16 | 3.12 | 2.46[a] | – |
| Width (km) | 1.09 | 1.24 | 1.09 | 1.71[a] | – |
| Depth (km) | 0.0[a] | 0.79 | 0.0[a] | 1.06[a] | 5.0[a] |
| Dip (°) | 46.7 | 12.3 | 46.7[a] | 0.0[a] | – |
| Opening (m) | 0.72 | 1.03 | 0.56 | 0.20 | – |
| ΔV ( × $10^6$ $m^3$) | 2.58 | 5.30 | 1.89 | 0.83 | −6.4 |
| RMS - GPS=5.92 cm; RMS - InSAR=3.32 cm | | | | | |

[a] Indicates parameters held fixed in the model optimization; ΔV stands for volume change

lost volume and is depressurized). The combined inflation rate from both reservoirs is also slightly higher after the eruption (3.7×$10^6$ $m^3$/year) than before the eruption (2.9×$10^6$ $m^3$/year). However, the volume estimates for the deep source are more uncertain, because its depth is relatively poorly constrained and there is a strong trade off between point-source depth and volume change (a point-source at greater depth requires more volume change to produce similar surface signals).

## Analysis of co-eruption deformation using GPS and InSAR data

Co-eruptive displacements in both GPS and InSAR data are dominated by the intrusion of the circumferential dike that fed eruptive fissures on the SW summit plateau. The two datasets observed significantly different parts of the deformation field, however. GPS data are mainly around the caldera rim where interferograms were mostly incoherent, whereas InSAR data provide displacements inside the caldera and on the volcano flanks, where no GPS stations exist. The largest LOS displacements in co-eruptive interferograms are up to 80 cm of uplift on the SW caldera floor, which is superimposed on broad subsidence that starts on the NE caldera floor and extends well outside the caldera (Fig. 4c–d).

Our first step in analyzing the co-eruption deformation is to correct the GPS displacements for pre-and post-eruption inflation (Table 1). To do this, we calculate the cumulative displacements at the GPS stations predicted by the pre- and post-eruption sill and point-source models (as discussed in the previous section), weight them to correct for the unequal

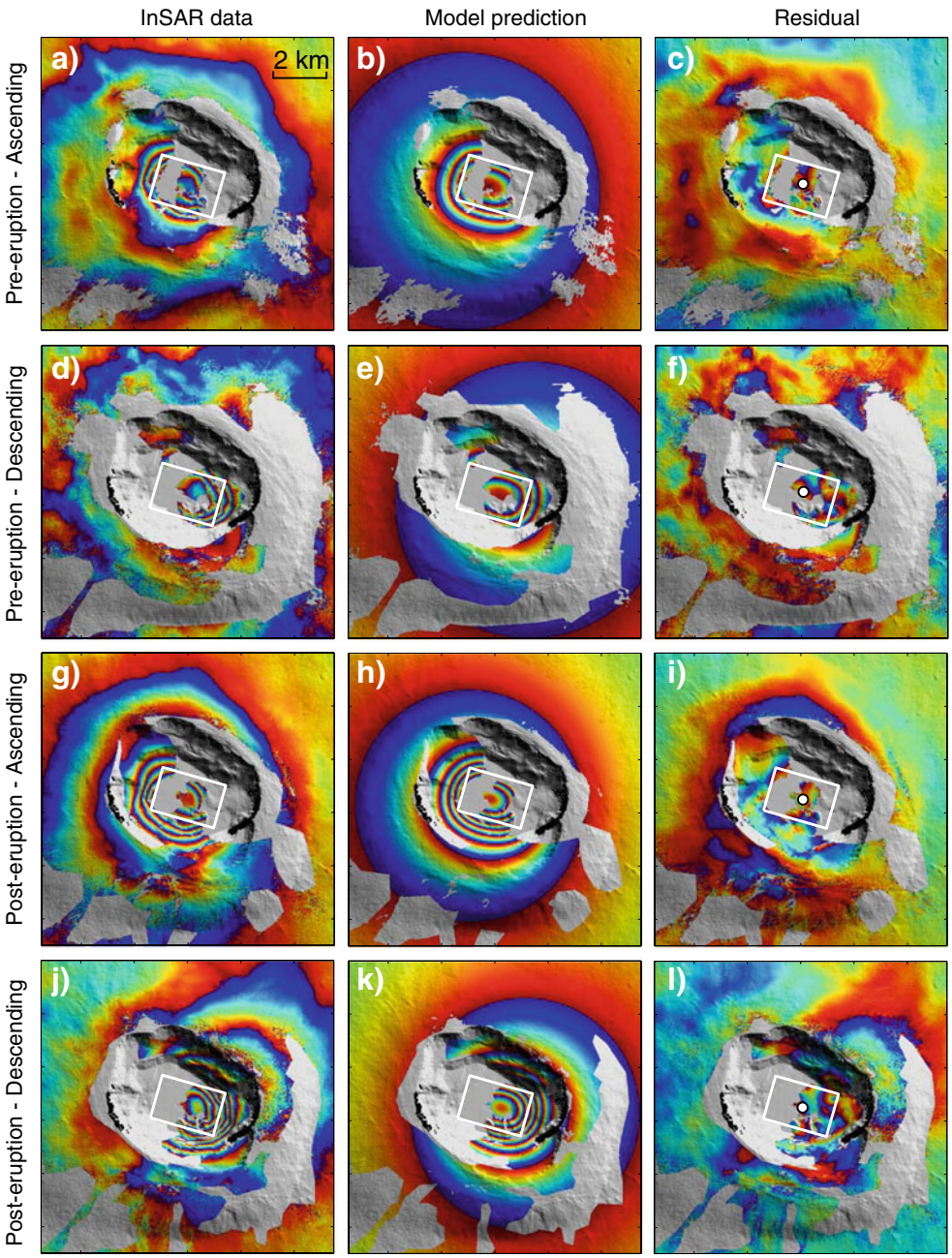


**Fig. 5** Modeling results of pre-eruption (**a**–**f**) and post-eruption (**g**–**l**) InSAR data, showing details near the caldera (left panels are observed; middle panels are model predictions; right panels are residuals). For each time interval, the line-of-sight (LOS) displacements from ascending and descending interferograms were combined and modeled together, but in this figure they are compared separately to the model results (**a**–**c** and **g**–**i** are ascending; **d**–**f** and **j**–**l** are descending). The models assumed a shallow sill and a deep point-source and solved for their sizes, positions, and depths. Both the pre- and post-eruption models yielded similar results (Table 3): sill and point-source positions near the center of the caldera with depths of ~1 km and ~5 km, respectively (white rectangles are the sill and white dots are the point-source; the latter only shown at right so as not to obscure information in the other panels). These source locations and dimensions were then held fixed in the co-eruption models (Figs. 6, 7, 8 and 9)

time intervals of the GPS and InSAR data (assuming fixed geometry and steady inflation rate), and then subtract those from the GPS displacements measured between June 2002 and July 2006 (Fig. 3). The resulting corrected GPS displacements are then used in the modeling of co-eruption deformation. Although the corrections are small at most stations, we did this to isolate the GPS displacements from the co-eruption time interval as much as possible so that they could be modeled together with the co-eruption InSAR data.

We assume that the two sub-caldera deformation sources determined from the pre- and post-eruption periods are also present during the co-eruption period; therefore, we hold their parameters fixed in the co-eruption modeling. To approximate the circumferential dike, we first introduced a planar dislocation with uniform opening (Okada 1985) whose top intersects the surface and has the same location, length, and strike as the 2005 eruptive fissures, but whose dip, amount of opening, and down-dip width could all vary. Initial results using this configuration had considerable mismatches between the observed and model displacements, and it became clear that it was difficult to satisfy both the GPS and InSAR data with such constraints. We therefore experimented with modeling the GPS data and the InSAR data separately, instead of combined, as a means of gaining insight into the geometry of the feeder dike to the 2005 eruption.

In the GPS-only case, the best-fit model yields a relatively thin (0.69 m) dike that is steeply dipping toward the caldera (58°) with a down-dip extent ("width") of 2.3 km, while the deep point source contracts by $-8.4\times10^6$ m$^3$ and the shallow sill expands by $20\times10^6$ m$^3$ (Table 4). This model fits the horizontal displacements at the GPS stations that straddle the 2005 eruptive fissure (FE06 & FE07) very well, but does not fit the vertical displacements there, nor the displacements at the far-field GPS stations (Data Supplement, Fig. S1). Further, the GPS-only model provides a poor fit to the InSAR data. In particular, the large expansion of the shallow sill creates a larger area of uplift in and around the caldera than is observed.

On the other hand, modeling only the InSAR data and requiring the dike to reach the surface as in the GPS-only case results in a best-fit dike that is also steeply dipping (56°), extends 2.8 km down-dip, and is very thick (2.3 m). This solution matches the InSAR data better but produces horizontal displacements near the eruptive fissure that were much larger than observed by GPS. If the model dike was not required to reach the surface in the InSAR-only case, and its length, width, and position were allowed to float, an even better fit to the InSAR data is achieved (Data Supplement, Fig. S2). In these results, the dike top is at a depth of 0.5 km, it has a gentle dip (26°), a length of 4.2 km (~1 km longer than the eruptive fissures), a down-dip width of 2.2 km, and a thickness of 1.0 m (Table 4). In this case, both the deep point source and shallow sill contract, by $-8.9\times10^6$ m$^3$ and $-0.3\times10^6$ m$^3$, respectively. Even though its position was not constrained, the best-fit dike was still located beneath the SW rim of the caldera. The model provides a reasonable fit to the InSAR data, but the predicted displacements at the GPS stations (particularly near the eruptive fissures) are much smaller than observed and in some cases are in the wrong direction (primarily because the model dike does not reach the surface). The horizontal displacements of the far-field GPS stations are matched well, however.

These initial results show that the better a one-dike model fits one dataset (either GPS or InSAR), the worse if fits the other. Furthermore, if the GPS and InSAR data are combined and modeled together, the best-fit model (with a single dike reaching the surface at the eruptive fissures) does not satisfy either dataset particularly well (Data Supplement, Fig. S3). The best-fit results for the combined dataset are a dike that dips gently (34°) toward the caldera with a down-dip width of 2.8 km and an opening of 1.0 m (Table 4). The vertical GPS displacement at FE06 is matched well, but not the displacements at the far-field stations, which seem to require a dike with a steeper dip. The contractions of the sub-caldera sources in this case are small: $-3.0\times10^6$ m$^3$ for the deep point source and $-0.6\times10^6$ m$^3$ for the shallow sill, which do not reproduce the island-wide subsidence signal very well. The poor agreement between these results and the data tell us that this configuration of model deformation sources (one dike and two sub-caldera sources) is not sufficient to explain the observed deformation.

However, these preliminary modeling experiments are informative. The best InSAR-only solution is a buried dike with a gentle dip, whereas the best GPS-only case is a steeper dike that reaches the surface, suggesting that a model that incorporates both these elements might better satisfy both datasets. In other words, a better model representation of the 2005 dike would be a curved or hinged dike with a steep portion near the surface and a more gently dipping section at depth, connected by a horizontal hinge line. Support for this idea comes from the observation that the displacements promoted by each of the separate GPS-only and InSAR-only models would help fill deficiencies in the other. For example, the greater uplift provided by the gentler-dipping dike in the InSAR-only case would help boost the insufficient near-field vertical displacements and the far-field horizontal displacements in the GPS-only model. Likewise, the greater horizontal displacements created by the steeply-dipping dike in the GPS-only case would remedy the lack of horizontal deformation in the InSAR-only model.

In order to test this idea, we performed additional model optimizations with the surface dike and the horizontal sub-caldera sill connected along horizontal hinge-lines by a third rectangular planar dislocation (Fig. 6). Physically, the deepest of the three rectangular sheets represents the sub-caldera sill, which is held fixed at the location determined by the pre- and post-eruption models. The two shallower sheets represent the dike that intruded from the sill to the surface, and whose dip increases toward the surface. The two dikes that connect the sill to the surface are constrained to have the same strike since they meet along hinge-lines, and in our initial run we fixed the dip of the surface dike to be 58°, the result from the GPS-only single-dike model (Table 4). The top edge of the surface dike is held at the location of the eruptive fissures. The other parameters float and are simultaneously estimated in the model optimization (surface dike down-dip width, hinge dike dip, hinge dike length, and amount of opening of both dikes; note the first two parameters are linked because the two dikes are physically connected). The results are a significant improvement on the single-dike model and reproduce the main features of the deformation pattern associated with the 2005 eruption, including the broad subsidence, the uplift near the eruptive fissures, and especially the near-field horizontal GPS vectors (Fig. 7, Table 4).

This model includes a slight inflation of the sub-caldera sill (Table 4), which seems physically unlikely because we

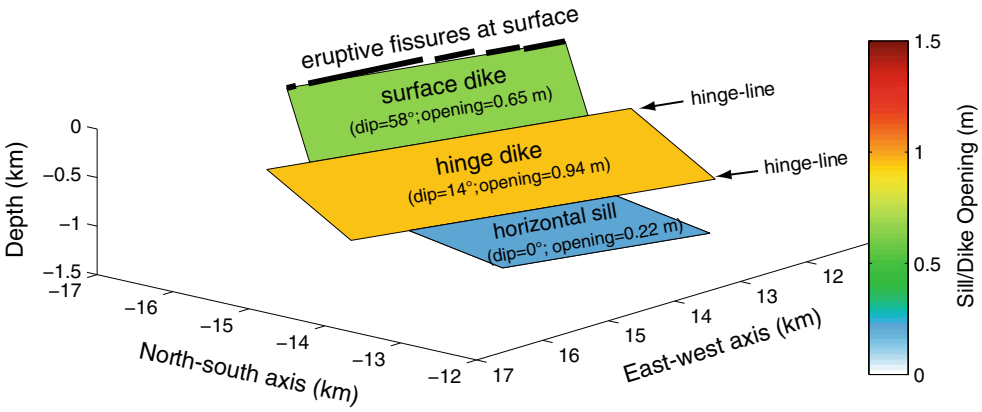


**Fig. 6** Three-dimensional view of sub-caldera sill and two dikes extending to the eruptive fissures at the surface (*bold lines, upper left*). Amount of opening of the sill and each dike segment are indicated by colors and are listed in Table 4

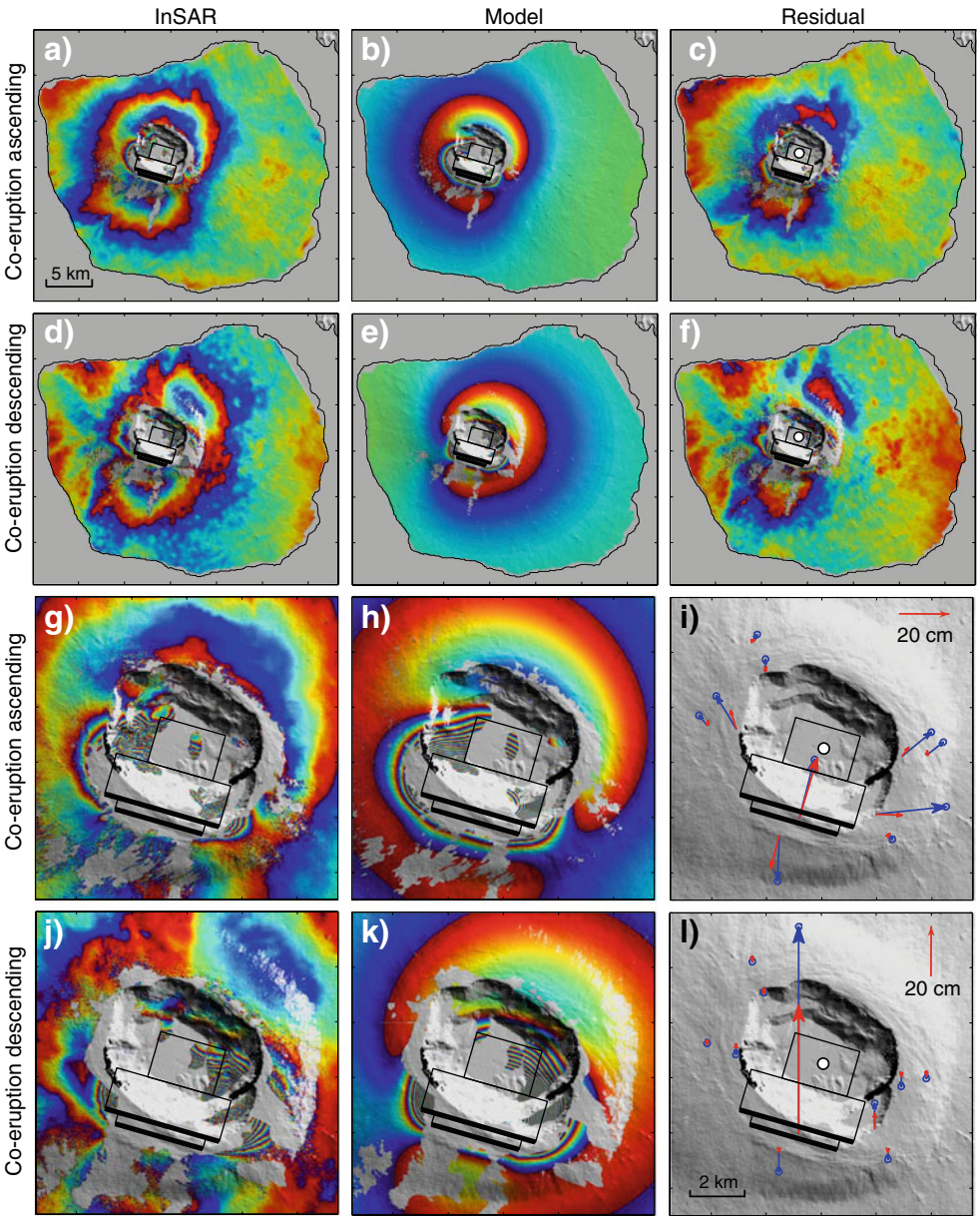


**Fig. 7** Model results of co-eruption deformation, using combined GPS and InSAR data and assuming two planar dikes connected to a sub-caldera sill, and underlain by a deep point source (Fig. 6, Table 4). (**a**–**c**) Ascending co-eruptive InSAR, (**d**–**f**) descending co-eruptive InSAR (data, model, residuals, respectively). (**g**–**h**) and (**j**–**k**) are the same as (**a**–**b**) and (**d**–**e**) but show more detail around caldera. (**i**) Horizontal and (**l**) vertical GPS displacements are shown by blue (observed) and red (model) vectors. Black rectangles in and around caldera show locations of sill and dikes (*bold lines* indicate upper edge); white dot (only shown at right) is deep point source

envision that magma was withdrawn from the sill during the co-eruption time interval. We suspect that this result is an artifact of our model geometry and is due to the fact that the two dikes do not produce enough uplift along the southern edge of the caldera in this configuration. If we force the sill and point-source to contract by the same amount as in the InSAR-only case (above), we get results very similar to those in Fig. 7; they seem to match the InSAR data slightly better visually (Data Supplement Fig. S4), but the RMS fit to the data is somewhat worse (Data Supplement Table S1). However, the pattern of uplift in the southern half of the caldera and subsidence in the northern half in these model results, which is also clear in the InSAR data, is strong evidence that the sill actually contracted during the co-eruption interval.

In the previous model runs, there was also evidence that the 2005 dike had a greater length than the eruptive fissures. For example, in models in which the surface dike length was not fixed, the solutions consistently extend the dike to the east, and this improved the agreement with the far-field GPS displacements and the uplift in the InSAR data east of the eruptive fissures (Data Supplement, Fig. S2). We therefore experimented with adding one additional model element: a third planar dike segment extending east from the surface dike underlying the eruptive fissures whose strike, length, width, and opening could be independently solved. This "east dike" was forced to connect to the east end of the surface dike, was constrained to share the same dip, and was modeled with its upper edge at the surface.

This final (preferred) model (Fig. 8) again significantly improves the agreement between the InSAR and GPS observations and the model predictions (Fig. 9 and Table 4). In this configuration, the surface dike segment underlying the eruptive fissures has a dip of 47°, a down-dip width of 1.1 km, and an opening of 0.72 m. The hinge dike below it, which connects to the sub-caldera sill, has a dip of 12°, a width of 1.2 km, and an opening of 1.0 m. The sill, again, opens slightly (by 0.20 m for an expansion of $0.8\times10^6$ m$^3$), whereas the deep point-source contracts by $-6.4\times10^6$ m$^3$. The "east" dike segment has a strike of 50°, a dip of 47°, and an opening of 0.56 m (Table 4). The combined volume of the three dikes in this model is $12\times10^6$ m$^3$, nearly the same as the volume of erupted lava ($14\times10^6$ m$^3$), but considerably larger than the volume of contraction in the deep point-source (presumably from lava withdrawal out of the sub-caldera magmatic system). One possible reason for this volume discrepancy is that the co-eruption interferograms on which this modeling is based span a time period of 2–4 months after the eruption, and so inevitably include post-eruption re-inflation that effectively reduces the deflation observed in the "co-eruption" InSAR data.

## Petrology of the 2005 lavas and relation to deformation models

Fernandina's historical lavas are homogeneous tholeiites with mineral phases that indicate equilibration and crystallization in a magma reservoir at <3 km depth (Geist et al. 1998; Allan and Simkin 2000). The small variations of isotopic and compatible element compositions suggest that replenishment of the shallow reservoir from below is semi-continuous (Allan and Simkin 2000). The pre- and post-eruption inflation detected by GPS and InSAR and the frequency of eruptions at Fernandina support the idea that deep recharge probably occurs more or less continuously.

Despite the fact that the northern end of the 2005 fissure erupted within 1 km of the top of the 1995 fissure, and the magmas presumably originate from the same sub-caldera chamber, the two lavas are strikingly different petrographically (Fig. 10). The 1995 lava has nearly 20% large and

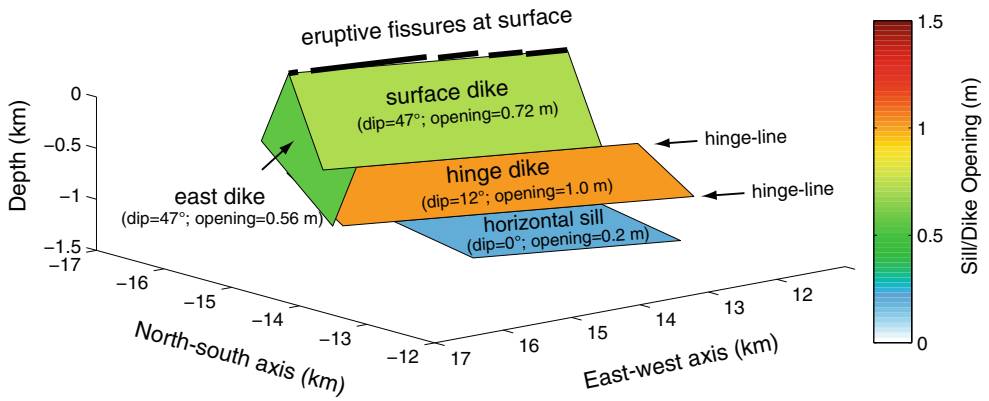


**Fig. 8** Three-dimensional view of sub-caldera sill and three dikes in preferred model for co-eruption deformation. A surface dike below the eruptive fissures (*bold lines, upper left*) is connected to the sub-caldera sill by a second dike along horizontal hinge lines. A third dike is located east of the eruptive fissures with a different strike. Amount of opening of each dike segment and in the sill are indicated by colors and are listed in Table 4. This model approximates a curved dike

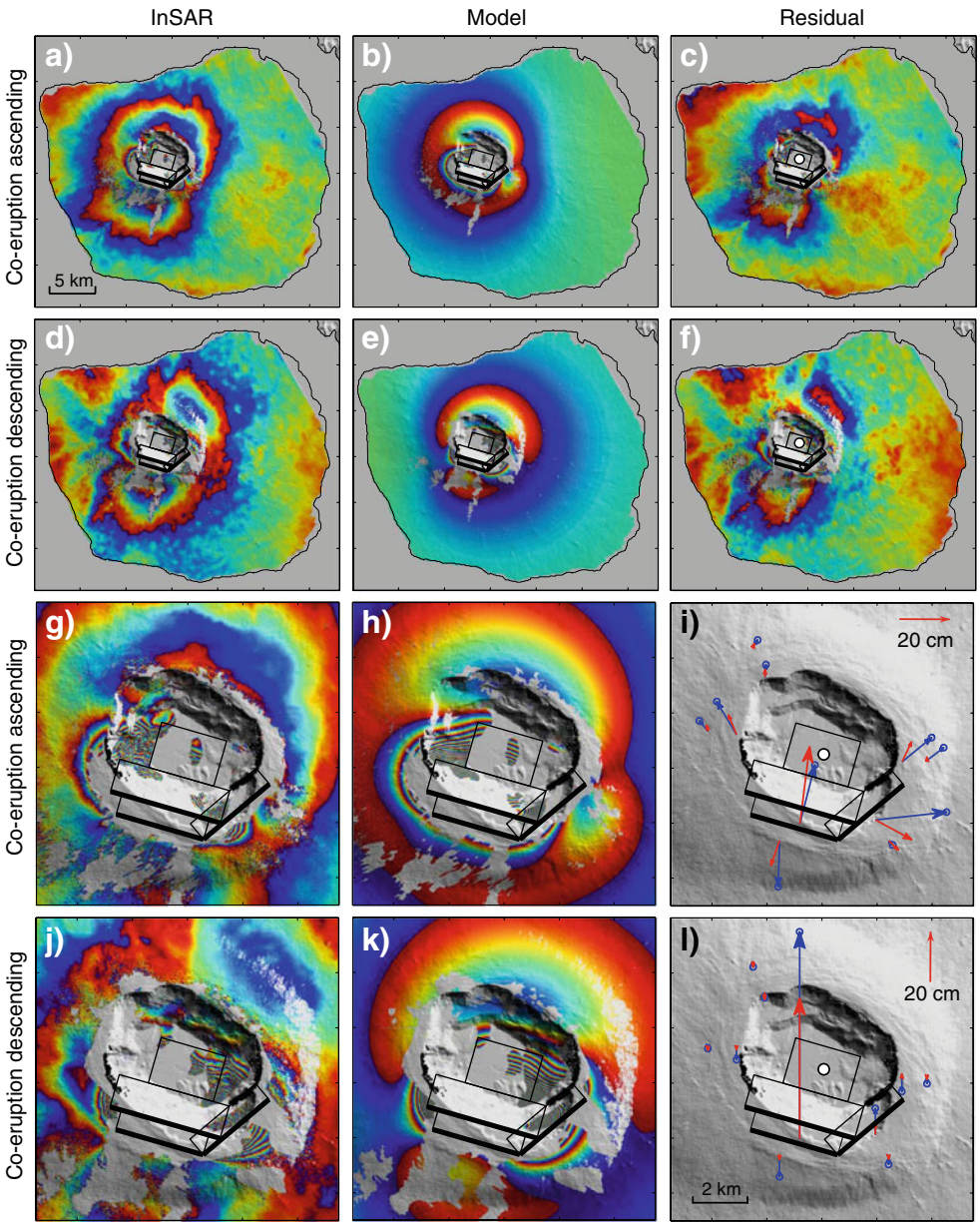


**Fig. 9** Preferred model results of co-eruption deformation, using combined GPS and InSAR data and assuming three planar dikes, a sub-caldera sill, and a deep point source (Fig. 8, Table 4). This model approximates a curved dike intruding from the sub-caldera sill to the surface. Individual panels as in Fig. 7

abundant phenocrysts of plagioclase (dominant), clinopyroxene, and olivine, whereas the early-erupted 2005 lava contains few phenocrysts >0.2 mm. Most crystals in the early 2005 lava are microlites and microphenocrysts with an acicular habit, which we believe indicates growth from the liquid shortly before eruption. The late-erupted 2005 lava contains up to 7% plagioclase phenocrysts and glomerocrysts, considerably less and with a distinctly more elongate habit than in the 1995 lava.

The 1995 and 2005 lavas define a small but distinct range compared to other Fernandina compositions (Fig. 11). The early 2005 aphyric lavas are indistinguishable from Fernandina submarine glasses (Geist et al. 2006b). Both the late 2005 porphyritic rocks and the 1995 lavas are richer in alumina than any submarine glasses with equivalent MgO

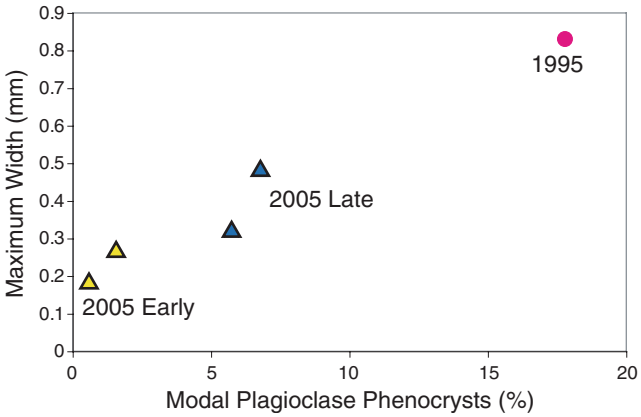


**Fig. 10** Petrographic features of 1995 and 2005 lavas, showing a wide variety of petrographic types

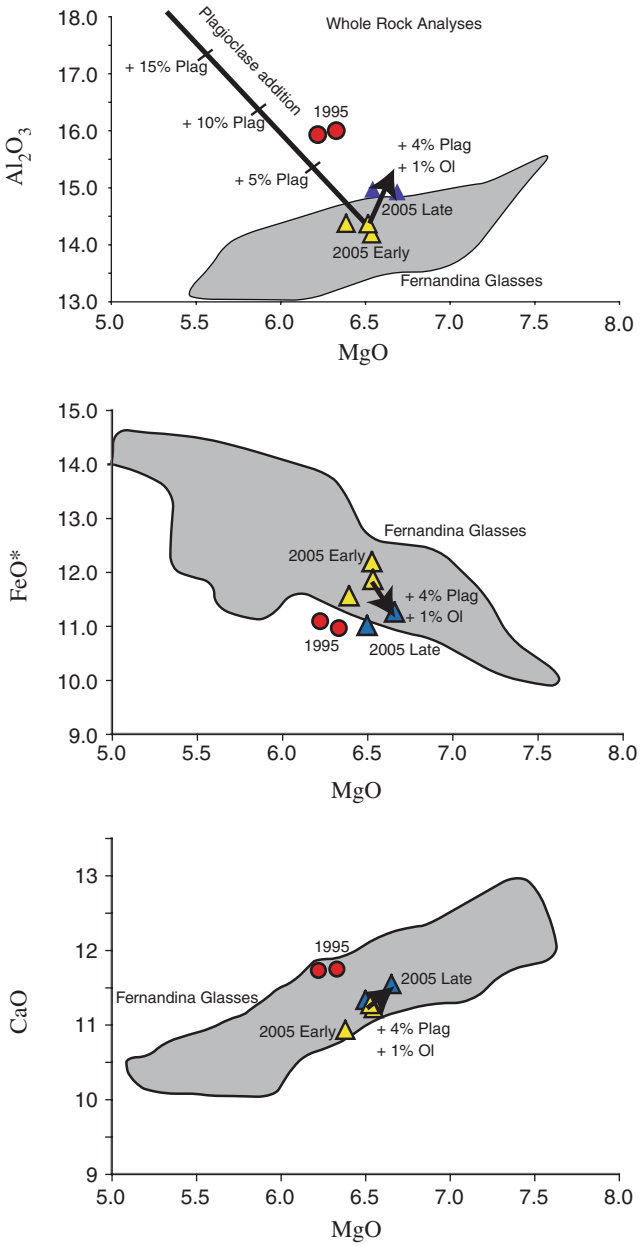


**Fig. 11** Compositions of 1995 and 2005 whole rock samples compared to Fernandina's submarine glasses (Geist et al. 2006b). Vector shows the compositional effect of adding 4% plagioclase and 1% olivine to a liquid whose composition is that of the aphyric early-erupted 2005 lava. *Line on top diagram* indicates the compositional effect of adding variable amounts of plagioclase

(Table 5). The late 2005 porphyritic lavas can be explained by the addition of 4% plagioclase and 1% olivine to the early 2005 composition (Fig. 11). Mass balance calculations indicate that little or no augite could be involved, because the CaO concentrations are similar in the early and late 2005 lavas.

These observations suggest that the aphyric early 2005 magma represents the liquid composition for the other lavas

**Table 5** Chemical compositions of 2005 Fernandina lava samples

| | MgO | $SiO_2$ | $TiO_2$ | $Al_2O_3$ | FeO* | MnO | CaO | $Na_2O$ | $K_2O$ | $P_2O_5$ | Ni | Cr | Sc | V | Ba | Rb | Sr | Zr | Y | Nb | Ga | Cu | Zn |
|---|---|---|---|---|---|---|---|---|---|---|---|---|---|---|---|---|---|---|---|---|---|---|---|
| Fe06 1 | 6.65 | 48.85 | 3.090 | 14.88 | 11.26 | 0.187 | 11.53 | 2.79 | 0.44 | 0.317 | 63 | 205 | 36 | 362 | 99 | 7 | 320 | 172 | 28 | 20.2 | 25 | 94 | 120 |
| Fe06 2 | 6.54 | 48.70 | 3.347 | 14.17 | 12.12 | 0.197 | 11.20 | 2.89 | 0.49 | 0.348 | 58 | 143 | 36 | 380 | 114 | 9 | 318 | 188 | 30 | 21.4 | 22 | 103 | 126 |
| Fe06 3 | 6.38 | 49.52 | 3.441 | 14.34 | 11.53 | 0.196 | 10.91 | 2.81 | 0.50 | 0.368 | 59 | 141 | 39 | 410 | 125 | 9 | 332 | 207 | 32 | 23.9 | 26 | 102 | 133 |
| Fe06 4 | 6.52 | 48.76 | 3.317 | 14.36 | 11.85 | 0.196 | 11.26 | 2.91 | 0.48 | 0.346 | 57 | 151 | 36 | 368 | 114 | 7 | 311 | 181 | 30 | 20.0 | 22 | 95 | 122 |
| Fe06 5 | 6.50 | 49.33 | 3.161 | 14.99 | 11.01 | 0.186 | 11.32 | 2.73 | 0.44 | 0.327 | 64 | 192 | 37 | 376 | 110 | 7 | 329 | 181 | 30 | 20.4 | 24 | 99 | 120 |
| | La | Ce | Pr | Nd | Sm | Eu | Gd | Tb | Dy | Ho | Er | Tm | Yb | Lu | Hf | Ta | Pb | Th | U | | | | |
| Fe06 1 | 14.3 | 34.9 | 4.94 | 22.0 | 5.54 | 1.86 | 5.81 | 0.92 | 5.39 | 1.08 | 2.90 | 0.38 | 2.37 | 0.32 | 3.85 | 2.3 | 0.89 | 2.3 | 0.4 | | | | |
| Fe06 2 | 16.1 | 39.0 | 5.54 | 24.8 | 6.28 | 2.09 | 6.55 | 1.06 | 6.07 | 1.23 | 3.30 | 0.45 | 2.72 | 0.38 | 4.47 | 1.7 | 1.04 | 2.6 | 0.4 | | | | |
| Fe06 3 | 17.2 | 41.5 | 5.90 | 26.1 | 6.57 | 2.16 | 6.75 | 1.09 | 6.18 | 1.25 | 3.39 | 0.45 | 2.69 | 0.38 | 4.43 | 1.5 | 1.10 | 2.6 | 0.4 | | | | |
| Fe06 4 | 16.4 | 39.6 | 5.61 | 24.9 | 6.35 | 2.10 | 6.58 | 1.05 | 6.06 | 1.23 | 3.28 | 0.44 | 2.65 | 0.37 | 4.38 | 1.8 | 1.05 | 2.3 | 0.4 | | | | |
| Fe06 5 | 15.0 | 36.5 | 5.20 | 23.3 | 5.93 | 2.00 | 6.18 | 1.00 | 5.73 | 1.17 | 3.11 | 0.43 | 2.57 | 0.37 | 4.25 | 1.5 | 0.98 | 3.0 | 0.4 | | | | |

Analyses by XRF by the method of Johnson et al. (1999). Measured precision is <2% RSD for all major elements and <5% for trace elements, except Sc (8%). Lower set of analyses are by ICPMS at Colgate University, using the methods of Harpp et al. (2003)

erupted in 1995 and 2005, which formed by addition of phenocrysts to this liquid. The trace elements help constrain this model (Fig. 12, Table 5). Compared to the earliest-erupted 2005 lava, late 2005 lavas are diluted in all incompatible trace elements by 10%, and they have positive anomalies of Sr and Ni. This is attributed to addition of plagioclase and olivine. The porphyritic 1995 lava also has positive Sr and Ni anomalies. It is richer in incompatible elements than all of the 2005 lavas, however, which we attribute to the injection of a liquid with lower incompatible trace element concentrations into the shallow magma chamber between 1995 and 2005.

These short-term variations in lava petrography and composition are consistent with models developed for the entire historical record at Fernandina (Allan and Simkin 2000) and the record on its submarine flanks (Geist et al. 2006b). The petrologic evidence suggests that the radial dike that erupted in 1995 propagated from the sub-caldera magma plumbing system from a greater depth than the 2005 dike. The 1995 dike eroded plagioclase-rich crystal mush from the margins of the magma supply system, causing the overall mode of plagioclase, and minor amounts of mafic minerals, to increase within the erupted lava. In contrast, the 2005 circumferential dike was emplaced vertically from the top of the magma supply system and did not encounter a substantial (deeper) mush zone. The notion that circumferential dikes originate from a shallower part of the sub-caldera magma reservoir and that radial dikes intrude from the deeper sides of the sub-caldera reservoir system is consistent with the earlier modeling results of Chadwick and Dieterich (1995).

## Discussion

From modeling of GPS and InSAR measurements, we draw a number of conclusions about the deformation associated with the 2005 circumferential dike intrusion and eruption at Fernandina. It is clear from the pattern of uplift during the pre- and post-eruption time intervals that magmatic inflation occurred in a shallow sill-like reservoir beneath the caldera at ~1 km depth. However, it is also apparent from the broader pattern of subsidence in the co-eruption time period, and from modeling of the pre- and post-eruption intervals, that a deeper magmatic source must also exist, and we model it as a point-source at ~5 km depth. The depth and geometry of the shallow source are better constrained than those of the deeper one. These two sub-caldera sources are included in all our co-eruption modeling, and this distribution of magma storage zones is consistent with the petrology of Fernandina lavas, especially if the zone between the shallow and deep magma chambers is occupied by a crystal mush. The pattern of pre- and post-eruption inflation, and co-eruption deflation, indicates that a hydraulic connection exists between the shallow and deep reservoirs and that recharge into the shallow reservoir from the deeper one is greatest immediately after eruptions when the pressure in the shallow reservoir is reduced and the pressure gradient from the deep reservoir is highest. The 1968 eruption at Fernandina was apparently an extreme example of co-eruption deflation, because it was followed by a major collapse of the caldera (Simkin and Howard 1970), suggesting an especially large volume

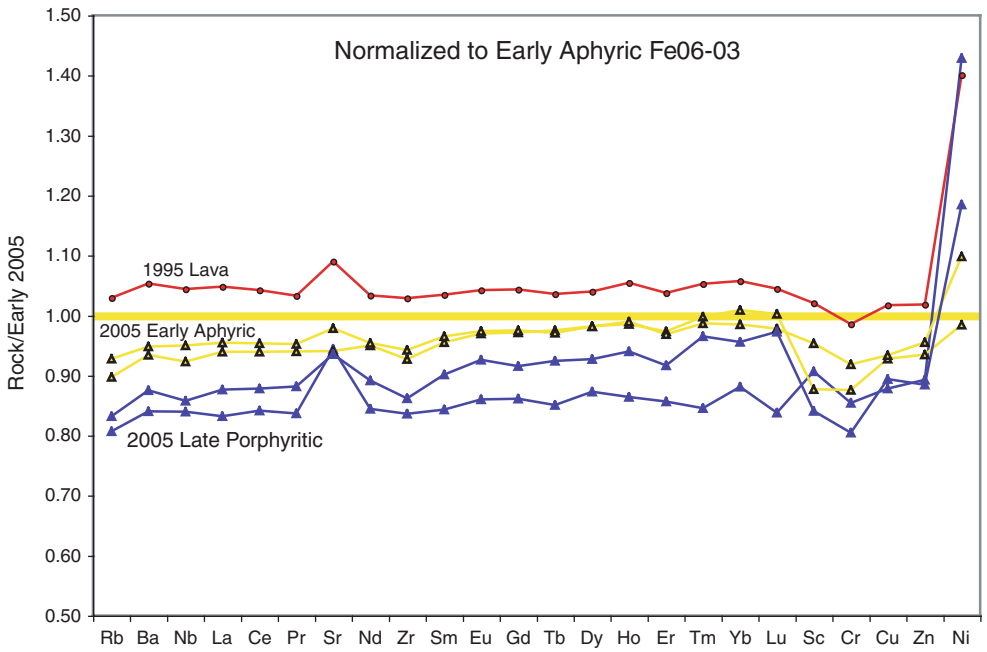


**Fig. 12** Trace element concentrations in 1995 and 2005 rocks, normalized to an aphyric early-erupted lava. Note the linear scale on the vertical axis

of magma was removed from the reservoir system (even though the subaerial erupted volume at the time was small). During circumferential eruptions, magma is removed mostly from the shallow reservoir, whereas radial eruptions apparently tap deeper portions of the magma supply system.

The 2005 co-eruption deformation is dominated by large dike-induced uplift focused on the SW caldera floor and rim, and is superimposed on a broader, caldera-centered subsidence that is smaller in magnitude but covers much of the island. This is consistent with magma leaving the sub-caldera storage reservoirs to feed the dike intrusion and eruption. The co-eruption GPS and InSAR displacements clearly show that the 2005 dike dips toward the caldera. This is reflected in the fact that inboard GPS station FE06 uplifted 84 cm, whereas outboard station FE07 subsided 9 cm (Table 1), and by the distribution of uplift and subsidence recorded by InSAR in and around the caldera. Our modeling indicates that the GPS displacements, especially near the eruptive fissures, are dominated by the shallow part of the dike, while the greater spatial coverage of InSAR reflects the deeper portions of the intrusion. A single planar dike cannot reproduce the deformation from both datasets. Adding multiple planar dikes to the models to simulate a curved dike that changes dip with depth, changes strike along the caldera rim, and is connect to one edge of the sub-caldera sill, provides a better fit to the combined GPS and InSAR dataset.

We therefore conclude that the shape of the 2005 dike is not a two-dimension plane as dikes are traditionally envisaged, but rather is more like a three-dimensional concave shell (Fig. 13). In other words, it is curved in both the vertical and horizontal dimensions, and its shape is presumably controlled by varying deviatoric stresses within the volcano. The inward dip of the dike decreases from 45 to 60° near the surface to 12–14° at a depth of ~1 km, where it intersects the top of the shallow sub-caldera sill from which it intruded. The trace of the dike in map view also curves around the caldera rim (Fig. 13). Curving circumferential eruptive fissures are observed at most of the active Galápagos volcanoes, although they commonly break up into *en echelon* segments at the surface (Chadwick and Howard 1991), as did the 2005 eruptive fissure. The remaining mismatch between our preferred co-eruption model and the data is at least in part due to the inherent limitations of using two-dimensional planar dike models to approximate the relatively complex three-dimensional curved shape of the 2005 feeder dike at Fernandina and perhaps also from the lack of topography in the models.

The 2005 eruption is the first geodetically-monitored circumferential dike intrusion in the Galápagos (or anywhere, so far as we know), so the geometry of the dike and the deformation associated with its emplacement are of particular interest. Our preferred model confirms some of the conclusions of Chadwick and Dieterich (1995), who investigated the stress field required to explain the pattern of circumferential and radial dike intrusion on Galápagos volcanoes. The shape of the 2005 circumferential dike from our modeling is similar to the stress trajectories in the dike intrusion model of Chadwick and Dieterich (1995), which included a dike extending from the outer corner of a flat-topped magma reservoir with a gentler dip at depth and a steeper dip at the surface. Our preferred model also shows that the amount of opening of the 2005 circumferential dike near the surface was modest (65–72 cm), suggesting that the levels of compressive stress perpendicular to the dike (in the direction radial to the caldera) were relatively high. This is consistent with Chadwick and Dieterich's (1995) argument that repeated circumferential intrusions should

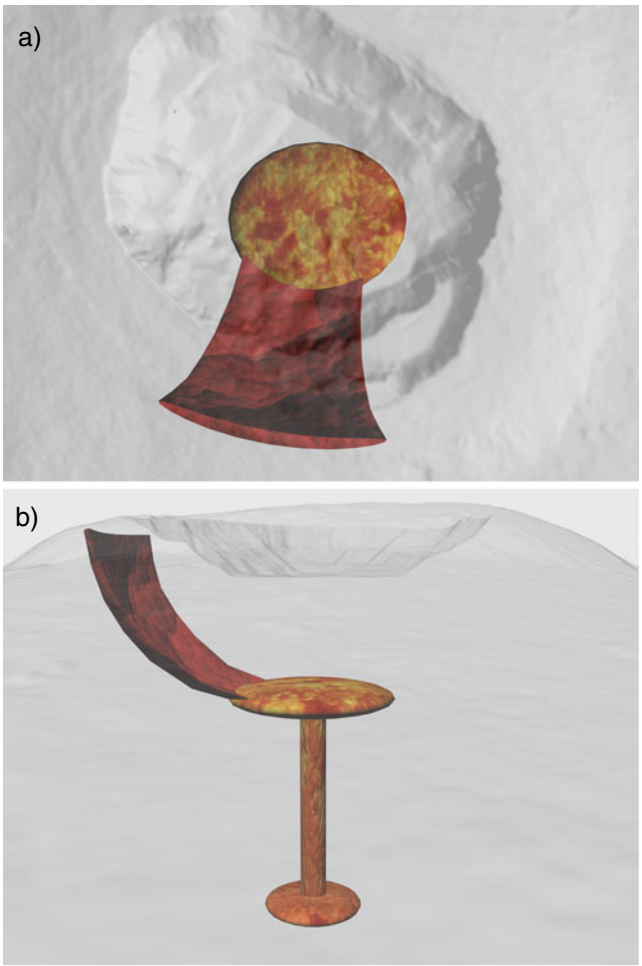


**Fig. 13** Three-dimensional representation of the sub-caldera magmatic system that fed the 2005 eruption at Fernandina, based on the results of this study. **a** View from above. **b** Oblique view from the side, looking northeast. A curved circumferential dike with the shape of a concave shell intrudes to the surface from a horizontal sub-caldera sill at 1 km depth, which is in turn underlain by a deeper magma reservoir at 5 km. Dike thickness not to scale. Illustration by Clay Hamilton

produce high levels of radial compressive stress in the absence of structural accommodation by slope failure or extensional faulting on the volcano flanks. The opening of the 2005 dike was mostly accommodated by horizontal displacements toward the caldera rather than away from it, as shown by the (corrected) GPS vectors at stations FE06 and FE07 (Fig. 3). This suggests that spreading of the summit platform toward the caldera leads to periodic slumping or avalanching of rim material into the caldera, as occurred in 1988 (Chadwick et al. 1991), and may be an important mechanism of long-term structural accommodation from repeated dike intrusion in the circumferential zone.

The modeling of Chadwick and Dieterich (1995) also suggested that a feedback relationship exists between circumferential and radial intrusions, because the stress changes caused by intrusions in one orientation tend to favor future intrusions in the other orientation. The record of recent eruptions on the SW flank of Fernandina seems to support this hypothesis, with alternating circumferential and radial eruptions in 1982 (circumferential), 1995 (radial), 2005 (circumferential), and most recently by another radial eruption in April 2009 (Smithsonian Institution 1995–2009). If this pattern continues, the next eruption on Fernandina will be from a circumferential dike intruded SW of the caldera.

**Acknowledgments** The manuscript was greatly improved by helpful reviews from Sang-Ho Yun and Scott Rowland. This research was supported by grants from the National Science Foundation Earth Sciences Program (EAR-9814312, EAR-0004067, and EAR-0538205), and in part by the NOAA Vents Program (PMEL contribution #3559). Michael Ramsey (University of Pittsburg) and Scott Rowland (University of Hawaii) kindly assisted with acquiring and processing the ASTER satellite imagery. ENVISAT radar data were provided by the European Space Agency through Cat-1 project #3493. Clay Hamilton at upwarp.com created the illustration in Fig. 13. The Charles Darwin Research Station and the Galápagos National Park Service provided invaluable logistical assistance. Beth Bartel, Erika Rader, Glyn Williams-Jones, Nathalie Vigouroux, Terry Naumann, and Kim Whipple helped in the field during our 2002 and 2006 GPS surveys. This paper is dedicated to the memory of our late friend, colleague, and co-author Daniel J. Johnson.

## References

Allan JF, Simkin T (2000) Fernandina Volcano's evolved, well-mixed basalts: mineralogical and petrological contraints on the nature of the Galapagos plume. J Geophys Res 105(B3):6017–6041

Amelung F, Jónsson S, Zebker H, Segall P (2000) Widespread uplift and 'trapdoor' faulting on Galápagos volcanoes observed with radar interferometry. Nature 407:993–996

Anderson EM (1936) The dynamics of the formation of cone sheets, ring-dikes and cauldron subsidences. R Soc Edinb Proc 56:128–163

Bagnardi M, Amelung F (2010) The shallow magmatic system of Fernandina Volcano, Galapagos Islands. Evidence of multiple magma reservoirs from Satellite Radar Interferometry. Eos Trans AGU 91(52), Fall Meet Suppl, Abstract G23C-0851

Bagnardi M, Amelung F, Baker S (2009) Deformation associated with 1995, 2005 and 2009 eruptions at Fernandina Volcano, Galápagos, observed by Satellite Radar interferometry. Eos Trans AGU 90(52), Fall Meet Suppl, Abstract G43C-01

Bailey EB, Maufe HB (1960) The geology of Ben Nevis and Glen Coe and the surrounding country. Memoir Geological Survey of Scotland 1–307

Chadwick WW Jr, Dieterich JH (1995) Mechanical modeling of circumferential and radial diking on Galapagos volcanoes. J Volcanol Geotherm Res 66(1–4):37–52

Chadwick WW Jr, Howard KA (1991) The pattern of circumferential and radial eruptive fissures on the volcanoes of Fernandina and Isabela Islands, Galapagos. Bull Volcanol 53:259–275

Chadwick WW Jr, De Roy T, Carrasco A (1991) The September 1988 intra-caldera avalanche and eruption at Fernandina volcano, Galapagos Islands. Bull Volcanol 53:276–286

Chadwick WW Jr, Geist DJ, Jónsson S, Poland M, Johnson DJ, Meertens CM (2006) A volcano bursting at the seams: inflation, faulting, and eruption at Sierra Negra Volcano, Galápagos. Geology 34(12):1025–1028. doi:10.1130/G22826A.1

Dvorak JJ, Okamura AT (1987) A hydraulic model to explain variations in summit tilt rate at Kilauea and Mauna Loa volcanoes. In: Decker RW, Wright TL, Stauffer PH (eds) Volcanism in Hawaii. U. S. Geol Surv Prof Pap 1350:1281–1296

Filson J, Simkin T, Leu LK (1973) Seismicity of a caldera collapse: Galapagos Islands 1968. J Geophys Res 78(35):8591–8622

Geist DJ, Naumann TR, Larson PL (1998) Evolution of Galápagos magmas: mantle and crustal fractionation without assimilation. J Petrol 39:953–971

Geist DJ, Chadwick WW Jr, Johnson DJ (2006a) Results from new GPS monitoring networks at Fernandina and Sierra Negra volcanoes, Galápagos, 2000–2002. J Volcanol Geotherm Res 150:79–97. doi:10.1016/j.jvolgeores.2005.07.003

Geist DJ, Fornari DJ, Kurz MD, Harpp KS, Soule SA, Perfit MR, Koleszar AM (2006b) Submarine Fernandina: magmatism at the leading edge of the Galápagos hot spot. Geochem Geophys Geosyst 7:Q12007. doi:10.1029/2006GC001290

Harpp KS, Fornari DJ, Geist DJ, Kurz MD (2003) Genovesa Submarine Ridge: a manifestation of plume-ridge interaction in the northern Galápagos Islands. Geochem Geophys Geosyst 4 (9):8511. doi:10.1029/2003GC000531

Hugentobler U, Schaer S, Fridez P (2001) Bernese GPS Software Version 4.2. Astronomical Institute, University of Berne, Berne, p 515

Johnson DM, P.R. H, Conrey RM (1999) XRF analysis of rocks and mineral for major and trace elements on a single low dilution Li-tetraborate fused bead. Adv X-Ray Anal 41:843–867

Johnson SE, Schmidt KL, Tate MC (2002) Ring complexes in the Peninsular Range Batholith, Mexico and the USA: magma plumbing systems in the middle and upper crust. Lithos 61:187–208

Jónsson S (2009) Stress interaction between magma accumulation and trapdoor faulting on Sierra Negra Volcano, Galápagos. Tectonophysics 471(1–2):36–44. doi:10.1016/j.tecto.2008.08.005

Jónsson S, Zebker H, Cervelli P, Segall P, Garbeil H, Mouginis-Mark P, Rowland S (1999) A shallow-dipping dike fed the 1995 flank eruption at Fernandina Volcano, Galápagos, observed by satellite radar interferometry. Geophys Res Lett 26(8):1077–1080

Jónsson S, Zebker H, Segall P, Amelung F (2002) Fault slip distribution of the 1999 Mw7.1 Hector Mine Earthquake, California, estimated from satellite radar and GPS measurements. Bull Seismol Soc Am 92:1377–1389

Jónsson S, Zebker H, Amelung F (2005) On trapdoor faulting at Sierra Negra volcano, Galápagos. J Volcanol Geotherm Res 144:59–71. doi:10.1016/j.jvolgeores.2004.11.029

Lu Z, Wicks C Jr, Dzurisin D, Thatcher W, Freymueller JT, McNutt SR, Mann D (2000) Aseismic inflation of Westdahl volcano, Alaska, revealed by satellite radar interferometry. Geophys Res Lett 27(11):1567–1570

McBirney AR, Williams H (1969) Geology and petrology of the Galapagos Islands. Geol Soc Am Memoir 118:197

Mogi K (1958) Relations between the eruptions of various volcanoes and the deformation of the ground surfaces around them. Bull Earthq Res Inst Univ Tokyo 36:99–134

Nooner SL, Chadwick WW Jr (2009) Volcanic inflation measured in the caldera of Axial Seamount: implications for magma supply and future eruptions. Geochem Geophys Geosyst 10:Q02002. doi:10.1029/2008GC002315

Okada Y (1985) Surface deformation due to shear and tensile faults in a half-space. Bull Seismol Soc Am 75:1135–1154

Okada Y (1992) Internal deformation due to shear and tensile faults in a half-space. Bull Seismol Soc Am 82:1018–1040

Rowland SK (1996) Slopes, lava flow volumes, and vent distributions on Volcan Fernandina, Galapagos Islands. J Geophys Res 101 (B12):27657–27672

Rowland SK, Harris AJL, Wooster MJ, Amelung F, Garbeil H, Wilson L, Mouginis-Mark PJ (2003) Volumetric characteristics of lava flows from interferometric radar and multispectral satellite data: the 1995 Fernandina and 1998 Cerro Azul eruptions in the western Galapagos. Bull Volcanol 65:311–330. doi:10.1007/s00445-002-0262-x

Ruiz A, Geist D, Chadwick WW, Jr. (2007) Inflation of Sierra Negra volcano since the 2005 eruption. Eos Trans AGU 87(52), Fall Meet Suppl, Abstract V53C-1422

Simkin T (1984) Geology of Galapagos Islands. In: Perry R (ed) Galapagos. Pergamon, Oxford, pp 15–41

Simkin T, Howard KA (1970) Caldera collapse in the Galapagos Islands, 1968. Science 169:429–437

Simkin T, Siebert L (1994) Volcanoes of the world. Geoscience, Tucson

Smithsonian Institution (1995–2009) Bulletin of the global volcanism network, Monthly reports for Fernandina volcano, http://www.volcano.si.edu/reports/bulletin/

Sudhaus H, Jónsson S (2009) Improved source modeling through combined use of InSAR and GPS under consideration of correlated data errors: application to the June 2000 Kleifarvatn earthquake, Iceland. Geophys J Int 176:389–404

Walker GPL (1993) Re-evaluation of inclined sheets and dykes in the Cuillins volcano, Isle of Skye. In: Prichard HM, Alabaster T, Harris NBW, Neary CR (eds) Magmatic processes and plate tectonics. Geological Society of London, Geol Soc Spec Pub 76:3–38

Yun S-H, Ji J, Zebker HA, Segall P (2005) On merging high- and low-resolution DEMs from TOPSAR and SRTM using a prediction-error filter. IEEE Trans Geosci Remote Sens 43(7):1682–1690

Yun S-H, Segall P, Zebker HA (2006) Constraints on magma chamber geometry at Sierra Negra Volcano, Galápagos Islands, based on InSAR observations. J Volcanol Geotherm Res 150:232–243. doi:10.1016/j.jvolgeores.2005.07.009

Zebker HA, Amelung F, Jonsson S (2000) Remote sensing of volcano surface and internal processes using radar interferometry. In: Mouginis-Mark PJ, Crisp JA, Fink JH (eds) Remote sensing of active volcanism. American Geophysical Union, Geophysical Monograph 116:179–206